Particle Actuation by Rotating Magnetic Fields in Microchannels: A Numerical Study

Seokgyun Ham[1], Wen-Zhen Fang[2], and Rui Qiao *[1]

[1]Department of Mechanical Engineering, Virginia Tech, Blacksburg, VA 24061, USA

[2]Department of Mechanical Engineering, National University of Singapore, 117575, Singapore

May 7, 2021

Abstract

Magnetic particles confined in microchannels can be actuated to perform translation motion using a rotating magnetic field, but their actuation in such a situation is not yet well understood. Here, the actuation of a ferromagnetic particle confined in square microchannels is studied using immersed-boundary lattice Boltzmann simulations. In wide channels, when a sphere is away from channel corners, it experiences a modest hydrodynamic actuation force parallel to the channel walls. This force decreases as the sphere is shifted toward the bottom wall but the opposite trend is found when the channel is narrow. When the sphere is positioned midway between the top and bottom channel walls, the actuation force decreases as the channel width decreases and can reverse its direction. These phenomena are elucidated by studying the flow and pressure fields in the channel-particle system and by analyzing the viscous and pressure components of the hydrodynamic force acting on different parts of the sphere.

*To whom correspondence should be addressed, email: ruiqiao@vt.edu.

1 Introduction

Manipulating microscale objects in a liquid environment is challenging. One of the reasons is that the motion of small objects is often governed by Stokes flows. A key characteristic of Stokes flows is that reciprocal movement of a "swimmer" in these flows cannot lead to a net displacement due to the time-reversibility in them, which is known as Purcell's scallop theorem.[1] Many techniques have been developed to manipulate microscopic objects in liquids, e.g., dielectrophoresis, diffusiophoresis, magnetophoresis, and so on.[2,3] Magnetism-based methods are popular because they are typically bio-compatible, e.g., magnetic fields can penetrate most media without adverse effects.[4–6] Magnetism-based particle manipulation methods can be broadly divided into two categories: driving particles using a net magnetic force and driving particles using a magnetic torque. For particles with a characteristic dimension r, the net magnetophoresis force they experience often scales as r^3,[7,8] and the induced translation speed scales with r^2.[9] Therefore, actuation based on net magnetic force typically requires very strong magnetic fields when the particle is small. Actuation based on magnetic torques, on the other hand, has more favorable scaling laws (e.g., the translation speed can scale with r)[10] and can provide large translation speed with weak or moderate magnetic fields. As such, torque-based magnetic actuation has attracted much attention in recent years.

To actuate microparticles using a magnetic torque, it is essential to break the time-reversal symmetry inherent in Stokes flow. Such a symmetry can be broken by using asymmetric geometry such as an artificial flagella or introducing a substrate.[11–16] Particles exhibiting magnetic torque-induced translation motion near substrates are often called surface walkers, and they are being studied intensively by many research groups.[10,17–22] Many interesting phenomena related to surface walkers have been discovered.[5,23–29] For example, when magnetic particles rotate above a solid wall, a chain of rotating particles travel faster than an individual particle rotating near the same wall;[19] hydrodynamic interaction between rotating particles can leads to particle clustering;[30] particle clustering can emerge spontaneously due to fingering instability in a swarm of particles;[31,32] rolling particles can exhibit flocking behavior at some frequencies of the applied magnetic field;[33] clusters of magnetic particles can be disassembled into shorter chains near uneven substrates using three-axis dynamic magnetic fields.[20]

Many potential applications of surface walkers require them to be actuated in confined spaces.[34,35] Therefore, it is worthwhile to study the dynamics of magnetic surface walkers under confined conditions. Research in this direction begins to receive attention only most recently, but some interesting phenomena have already been reported. For instance, the reversible response of superparamagnetic particles confined in a microchannel has been analyzed. It was found that the particle assembly is reconfigurable and the shape of the particle assembly depends strongly on the channel-particle size ratio.[36] The rheology of a sphere particle suspension confined between two plates under an external uniform magnetic field was studied. It is discovered that the magnetic torque applied to the sphere is transmitted to the fluid via viscous force, and consequently, the induced shear stress drives a unidirectional flow of the suspension.[37]

Understanding the actuation of magnetic surface walkers, or more generally, dynamics of magnetic particles in fluids, using experiments alone is challenging. Computational modeling is a powerful tool to complement experimental investigations. In the literature, many different methods, including Stokesian dynamics,[38] dissipative particle dynamics,[39] finite element method,[40,41] smoothed particle hydrodynamics,[42,43] and lattice Boltzmann method (LBM),[44,45] have been developed to investigate the dynamics of magnetic particles suspended in liquids. Using LBM, we recently studied the dynamics of surface walkers confined between two infinite walls.[46] It was found that the degree of confinement and the nature of the confining walls (slip vs no-slip) not only affect the speed of a sphere actuated by a rotating field, but also its direction. For example, for a sphere positioned at a fixed height above a lower no-slip wall, as the no-slip upper wall is brought closer to the lower wall, the translation of the sphere first slows down, then reverses direction, and finally reaches zero when the sphere is exactly in the middle way between the two walls.

While existing studies provided useful insights into the effects of confinement on the actuation of magnetic surface walkers by rotating fields, the confinement considered so far is usually afforded by two parallel walls that are normal to the rotating axis of surface walkers. In practice, a surface walker may be confined in more complex environment such as inside a channel with a finite aspect ratio. Understanding the actuation of surface walkers in such environment is useful for harnessing them for applications such as drug delivery through capillaries.[47] However, research on this is scarce at present. In particular, how the confinement by walls normal to the sphere's axis of rotation changes the fluid flow and actuation force has not been studied and is poorly understood. In this work, we investigate the actuation of a spherical surface walker confined in a square-shaped microchannel. The flow field and actuation force acting on the sphere in the channel length direction are computed numerically by varying the position of the sphere inside the channel and the dimension of the microchannel. The variation of the net actuation force is elucidated by examining its various components and the flow fields inside the microchannel.

2 Models and Methods

2.1 Physical and mathematical models

As shown in Fig. 1, the simulation system consists of a ferromagnetic sphere and a water-filled square channel, in which the sphere is immersed. The sphere has a radius of r. The channel has a width of W and a length of L. The sphere is positioned at a distance a and b from the bottom wall and the purple-shaded side wall, respectively. The bottom channel wall is in the xy-plane and the side channel wall is in the xz- plane. Under the action of an external magnetic field B, the sphere rotates around the z-axis in the clockwise direction. If the sphere is free, it may move in all three directions, which changes its confinement by the channel walls (i.e., a and b) and complicates the study of how confinement affects its actuation. To circumvent this problem, as is widely practiced,[48–50] the sphere is allowed to rotate but its center is fixed. The rotation-induced hydrodynamic force acting on the sphere in the x-direction, F_x, is measured as the actuation force.

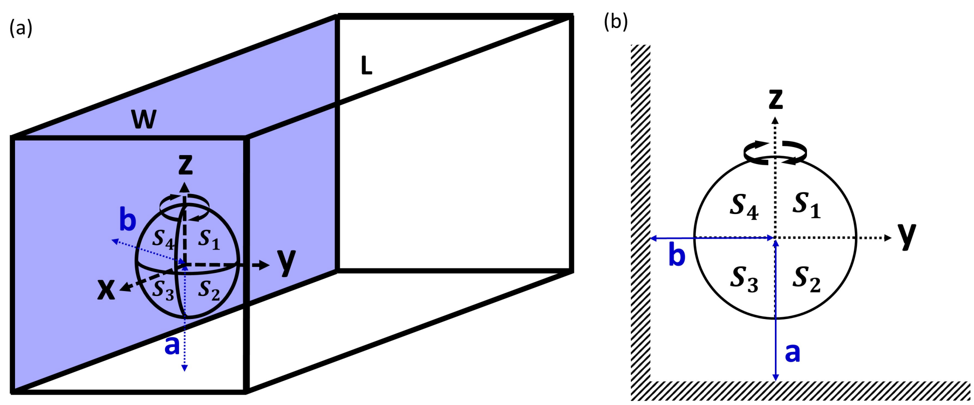

Figure 1: A three-dimensional view (a) and side view (b) of the system used to study the actuation of a magnetic sphere in a square channel. The sphere surface is divided into S_1, S_2, S_3, and S_4. In (b), only the channel walls closest to the sphere are shown. The origin of the coordinate system is set on the sphere's center.

Without losing generality, the sphere's radius is set to $12\mu m$. Its magnetic moment is $\boldsymbol{m} = 1.45 \times 10^{-10} \mathrm{A{\cdot}m^2}$. A magnetic field $\boldsymbol{B} = B\cos(2\pi f_B t)\boldsymbol{i} - B\sin(2\pi f_B t)\boldsymbol{j}$ is applied, where B is the strength of the magnetic field and f_B is the rotational frequency. B and f_B are set to 3 mT and 20 Hz, respectively. With the above parameters, the sphere rotates synchronously with the magnetic field in all of our simulations. The rotational Reynolds number $Re_\omega = 2\pi\rho f_B r^2/\mu = 4.52 \times 10^{-3} \ll 1$.

We note that the sphere also experiences forces in the $y-$ and $z-$directions. These forces can change the position of a free particle across the channel, but they are much weaker. Specifically, $F_x \sim \pi\mu\omega r^2$.[48,50,51] Forces in the $y-$ and $z-$directions (F_y and F_z), unlike F_x, originate from inertia effects and scale as $F_{y,z} \sim \pi\rho\omega^2 r^4$,[46,50] i.e., $F_{y,z}/F_x \sim Re_\omega$. Because $Re_\omega =\ll 1$, inertia effects are negligible and F_y and F_z are very small. In addition, other forces (e.g., Brownian forces) in those directions may be more important in understanding how a particle is driven away from walls. For these reasons, we will not elaborate on F_y and F_z. Because a free particle can depart from its initial position relative to channel walls due to non-zero $F_{y,z}$, we study the implications of such departure by examining how F_x varies with a and b in Fig. 1.

Three series of systems are studied to probe the effects of confinement on actuation by channel walls (see Table 1). In all systems, the sphere is positioned at a distance $b = 1.5r$ from the purple-shaded side wall. This distance is chosen so that particle actuation can be effectively studied using direct numerical simulations. For surface walkers, the actuation force decreases rapidly as b/r increases. Hence, a small b/r is preferred. However, if b/r is too small, resolving the flow between the sphere and wall necessitates an extremely fine grid and high computational cost. With $b = 1.5r$, our tests showed that a strong actuation force is generated and the force can be computed accurately using a reasonably fine grid (see below). The channel length is selected to $60r$ to minimize the finite size effects.[46] In the first series of systems, the channel is wide ($W = 6.5$-$30r$) and the sphere is fixed at various distances above the bottom wall to study the actuation near walls of a wide channel. In the second series of systems, the sphere is positioned midway between top and bottom walls while the channel width is varied to study the actuation with symmetric top/bottom walls. In the third series of systems, the channel is narrow ($W = 3.5 - 6r$) and the sphere is fixed at 1.2-3r above the bottom wall to study the actuation near walls of a narrow channel.

Table 1: A summary of the simulations performed in this study.

Series	a	b	W	L
1	$1.2r$ to $W/2$	$1.5r$	6.5 to $30r$	$60r$
2	$W/2$	$1.5r$	3 to $30r$	$60r$
3	$1.2r$ to $W/2$	$1.5r$	3.5 to $6r$	$60r$

The fluid motion is governed by the Navier-Stokes (NS) equations:

$$\frac{\partial \rho}{\partial t} + \nabla(\rho \boldsymbol{u}) = 0 \qquad (1)$$

$$\frac{\partial \rho}{\partial t} + \nabla(\rho \boldsymbol{u}\boldsymbol{u}) = -\nabla p + \nabla[\mu(\nabla \boldsymbol{u} + (\nabla \boldsymbol{u})^T] + \boldsymbol{F} \tag{2}$$

where ρ is the fluid density, $\boldsymbol{u}$ is the velocity, p is the pressure, μ is the viscosity, and $\boldsymbol{F}$ is the body force. The no-slip boundary condition is imposed on channel walls and the sphere's surface. The periodic boundary condition is imposed in the $x-$direction. The sphere's rotation is governed by

$$I_p \frac{d\boldsymbol{\omega_p}}{dt} = \int_s (\boldsymbol{X_s} - \boldsymbol{X_p}) \times (\sigma \cdot \boldsymbol{n}) ds + \boldsymbol{m} \times \boldsymbol{B} \tag{3}$$

where I_p is the sphere's moment of inertia, $\boldsymbol{\omega_p}$ is the sphere's angular velocity, σ is the fluid stress tensor, $\boldsymbol{n}$ is the unit normal vector of the sphere's surface, $\boldsymbol{X_s}$ and $\boldsymbol{X_p}$ denote the sphere's center and position on the sphere's surface, respectively. Equation 3 is solved together with Eq. 1 and 2 to compute a sphere's rotation. For the rotating magnetic field considered in this work, our simulation shows that the sphere rotates synchronously with the applied magnetic field.

2.2 Numerical methods and code validation

The mathematical models described in the previous section are solved by combining the LBM and the immersed boundary method (IBM).[52,53] These methods and their implementation have been described in details in our recent publication.[46] Here we highlight the salient features of these methods and present key implementation details.

The NS equations are solved using LBM. In LBM, evolution equations of the density distribution function, which can recover to the NS equations via the Chapman−Enskog expansion, are solved on a Eulerian lattice to obtain the fluid's density and velocity fields. The basic operations in LBM are the collision step and the streaming step. In the collision step, the distribution function components on each lattice is computed. In the streaming step, the post-collision distributed functions are spread to neighbor lattices by following designated microscopic velocity vectors. Because collision and streaming are local operations, LBM is highly efficient and easily parallelized.

The interactions between fluids and the solid sphere are handled using a fixed-grid method IBM.[53] Briefly, each solid boundary is represented using a set of Lagrangian forcing points and the flow field is solved on the Eulerian lattice, which covers both inside and outside of the solid boundary. The velocity of Lagrangian points on the solid boundary is interpolated from adjacent Eulerian lattice points through a discrete delta function. Meanwhile, the force density evaluated on Lagrangian points is spread to nearby Eulerian lattice points through the same discrete delta function. These treatments enforce the no-slip condition on the solid boundary and allow the effects of solid boundary on fluid flow to be modeled.

When implementing LBM, we adopt the three-dimensional 19-velocity (D3Q19) multi-relation-time scheme to solve the evolution equations[54–56]

$$g_\alpha(\boldsymbol{x} + \boldsymbol{e}_\alpha \delta t, t + \delta t) - g_\alpha(\boldsymbol{x}, t) = -(\boldsymbol{M^{-1} \Lambda M})_{\alpha\beta}[g_\beta - g_\beta^{eq}] + \delta t F_\alpha, \alpha = 0 \cdots 18 \tag{4}$$

where g is the density distribution function, $\boldsymbol{e}_\alpha$ is the discrete velocity along the α direction, and $\boldsymbol{\Lambda}$ is the collision matrix. The free relaxation parameter related to the kinematic viscosity is set to 1.25 while others are set to 1. The hydrodynamic force acting on fluids due to fluid-sphere interactions is treated using the techniques developed by Guo et al[57] and Kang et al.[53] The no-slip wall boundary condition is enforced using the halfway bounce-back scheme.[56] A uniform lattice spacing of $r/6$ is used to solve the Eq. 4. For the systems listed in Table 1, the total number of grid points ranges from 160,000 to 12,000,000, and there are at least two lattice points in the gap between the sphere and the wall (corresponding to $a/r = 1.2$). Grid-dependence is tested by comparing actuation force in representative cases with that obtained using a finer grid of $r/10$, with a deviation less than 2%. When implementing IBM, the sphere's surface is discretized into 536 Lagrangian nodes according to the method proposed by Feng et al,[52] leading to the spacing between neighbor Lagrangian nodes approximately equal to that between the Eulerian lattices.[52,56] The range of kernel function (Dirac delta distribution) to deal with the fluid-solid interaction function is twice the lattice spacing.

A code implementing the above methods has been developed and validated extensively for actuation of spherical surface walkers.[46] First, the rotation of a magnetic sphere driven by a rotating field in a unbounded fluid was simulated. The evolution of the sphere's rotation speed as a function of the field frequency, including the transition from the synchronous regime to the asynchronous regime, was accurately captured. Next, the hydrodynamic forces experienced by a sphere enclosed between two no-slip walls separated by $30r$ were studied systematically. When the domain size reaches $60r$ in the longitude direction and $30r$ in the transverse direction, the computed drag acting on a sphere translating near the lower wall agrees well with the analytical prediction for spheres moving parallel to a semi-infinite wall.[48] The hydrodynamic forces acting on a center-fixed sphere rotating at a height of $1.5r$ above the lower wall computed by the code converges within $\sim 5\%$ of the analytical predictions by Goldman and colleagues.[48,50]

3 Results and Discussion

Here we study the hydrodynamic actuation force experienced by a magnetic sphere inside a square channel under the actuation of a rotating magnetic field. As mentioned in Section 2.1, we let the sphere rotate around the $z-$axis in the clockwise direction but fix its center. We measure the hydrodynamic force on the sphere in the x-direction. Figure 2 summarizes the actuation force F_x, for the various a and W listed in Table 1. We observe that, in a very wide channel (e.g., $W = 30r$), when the sphere is away from the corner (e.g., $a = 15r$), F_x is positive as shown in prior works,[46,50] but becomes negative as the sphere is shifted toward the bottom wall (i.e., as r/a increases). In addition, as a sphere is shifted toward the bottom wall, F_x decreases if the channel is wide but increases when the channel is narrow ($W <\sim 6r$). These phenomena are examined in details in Sections 3.1 and 3.3, respectively. When the sphere is positioned midway between the top and bottom channel walls, F_x decreases as the channel width decreases and becomes strongly negative when the sphere becomes highly confined by the channel, and sharply recovers to zero when the symmetry is reached at $W = 3r$ and $a = 1.5r$. This series of study is discussed in Section 3.2.

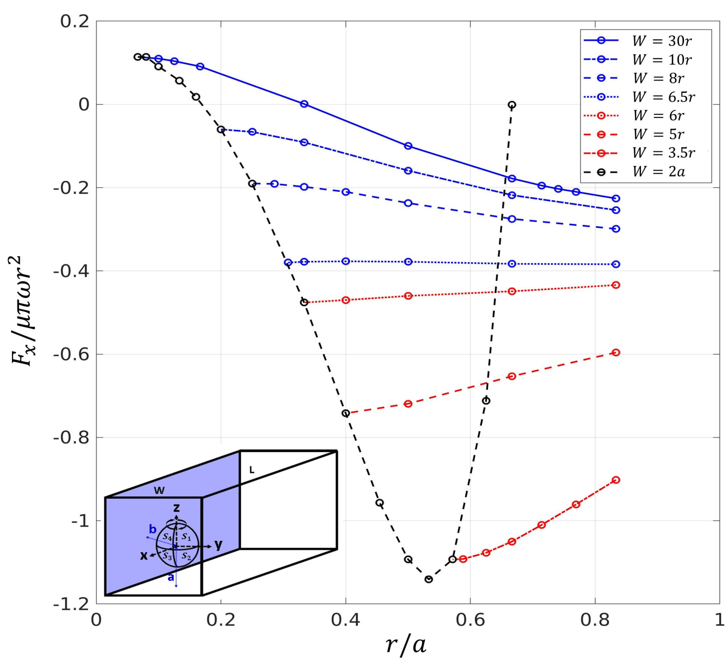

Figure 2: The evolution of the $x-$direction hydrodynamic actuation force on a rotating sphere as a function of channel width W and the sphere's distance from the bottom channel wall a. The blue, red, and black lines correspond to the Series 1, 3, and 2 simulations in Table 1.

3.1 Sphere actuation near walls of a wide channel

For the system shown in Fig. 1, the situation with $W \gg r$ and $a \gg r$ (i.e., when a sphere is positioned close to a semi-infinite vertical wall), has been studied in the literature.[10,46] Here, we set the sphere at a distance $b = 1.5r$ from the purple-shaded vertical wall and position the bottom wall at a distance a beneath the sphere. To understand how the sphere's actuation is affected by the corner formed by the bottom and side walls of a wide channel, we focus our discussion on a representative set of simulations where W is set to $30r$ and a is varied from $15r$ to $1.2r$.

We first examine the flow and pressure fields in two sample cases with $r/a = 1/15$ and $1/1.5$. Figure 3 show sample streamlines in the channel. At $r/a = 1/15$, when there is little confinement by the bottom wall, the rotating sphere induces a global flow in the channel in the positive $x-$direction (see Fig. 3a). Fluids are drawn toward the vertical wall on one side of the sphere and ejected away from the wall on the other side of the sphere (marked by red arrows). This global flow is accompanied by two recirculations, one primarily in the horizontal plane (marked by a black arrow) and one primarily in the vertical plane (marked by a blue arrow). Because the global flow is in the positive $x-$direction, hereafter, upstream of the sphere refers to the space in which $x < 0$ while downstream refers to the space in which $x > 0$.

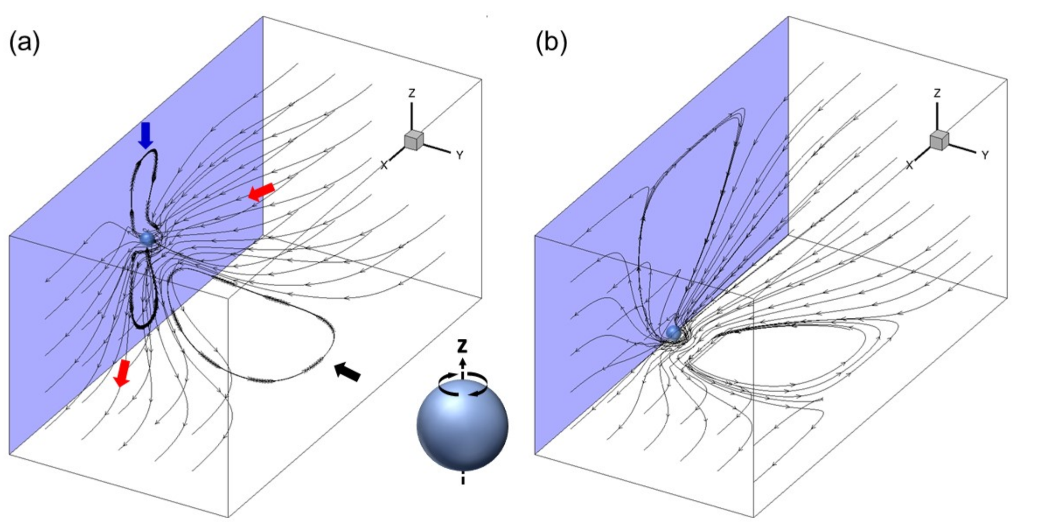

Figure 3: Sample streamlines in two channel-particle systems with $r/a = 1/15$ (a) and $r/a = 1/1.5$ (b). $W = 30r$ and $b/r = 1.5$ in both systems.

At $r/a = 1/1.5$, when there is significant confinement by the bottom wall, Fig. 3b shows that the basic features of the flow field remain similar, e.g., a global flow in the positive $x-$direction and recirculations still exist. Nevertheless, the additional confinement by the bottom wall leads to important differences from those shown in Fig. 3a. First, the bending of streamlines toward and away from the vertical wall becomes somewhat stronger. Practically, because there are often many particles in a channel, this effect makes it easier to entrain other particles toward a rotating particle located near a channel corner (note that the trajectory of entrained particles may differ from the streamlines showed here if the particle density in the channel is not low). This can be useful because the motion of an entrained, passive particle (e.g., a biological cell), once close enough to the rotating particle, can be controlled indirectly by manipulating the rotating sphere (e.g., push and pull of cells by a magnetic particle rotating near a semi-infinite wall have been demonstrated in recent experiments).[17] Second, in the horizontal plane, the recirculation zone moves closer to the sphere, which tends to increase the velocity gradient near the sphere's surface that faces away from the vertical wall. As we shall see later, this contributes to the reversal of the hydrodynamic actuation force on the sphere as r/a increases from 1/15 to 1/1.5.

Figure 4 shows the pressure field in the horizontal ($z = 0$) and vertical ($y = 0$) planes passing through the sphere's center for $r/a = 1/15$ and 1/1.5. As shown in Fig. 4a, at $r/a = 1/15$, where the confinement by the bottom wall is negligible, the confinement of a rotating sphere by the vertical wall induces a heterogeneous pressure field in the channel. Specifically, the rotating sphere draws fluids on one of its sides toward the wall to rise the pressure there (region A in Fig. 4a's inset) but reduces the pressure on its other side (region B in Fig. 4a's inset). This, along with the recirculation of fluids near the sphere, cause the fluid pressure to rise on one side of the sphere and to decrease on the other side. Examination of the pressure fields in the $z = 0$ and $y = 0$ planes (see Fig. 4a and 4c) reveals that the recirculation-induced pressure heterogeneity exists in a region up to many r from the sphere, which is consistent with the global flow shown in Fig. 3a. On the sphere's surface facing the vertical wall (S_3 and S_4), this kind of pressure heterogeneity creates a net force pushing the sphere in the negative $x-$direction.[46,50]

The global flow generated by the rotating sphere and its interactions with the *center-fixed* sphere, however, create a opposite pressure force on the sphere. Specifically, the pressure on the sphere's upstream surfaces is enhanced by the global flow, while the opposite occurs on the sphere's downstream surfaces. As shown in the inset of Fig. 4a, on the sphere's surface facing the vertical wall, this pressure imbalance by the global flow is weaker compared to the recirculation-induced pressure imbalance; however, on the sphere's surface facing away from the vertical wall, this pressure imbalance dominates and creates a net pressure force in the positive $x-$direction.

When the rotating sphere is positioned close to the bottom wall with $r/a = 1/1.5$, Fig. 4b

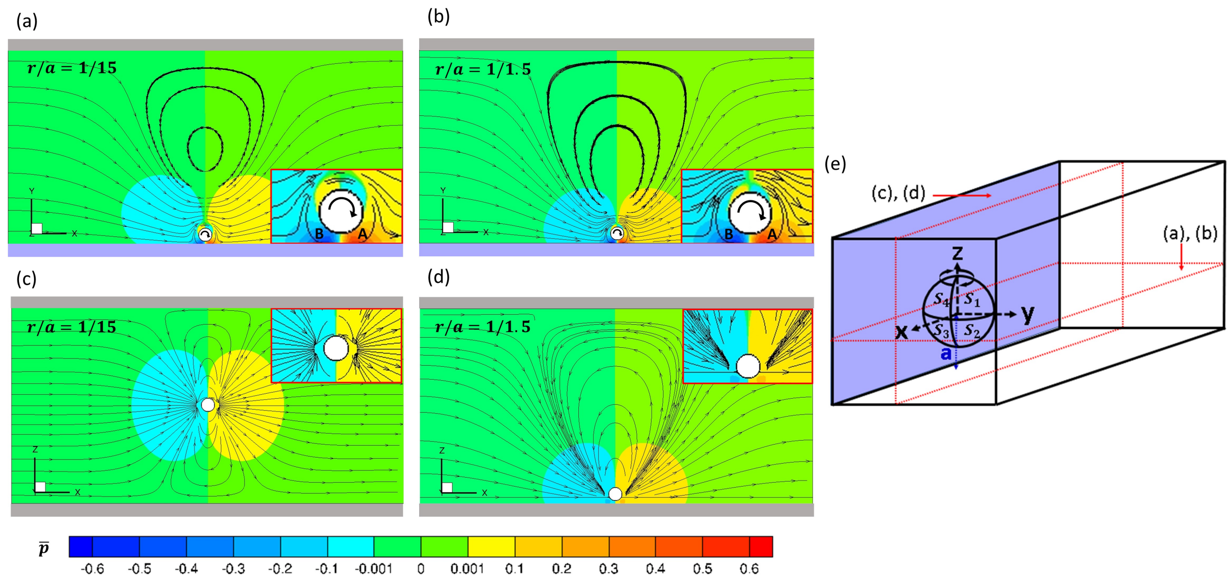

Figure 4: Pressure field and streamlines in channel-particle systems with different r/a but same $b/r = 1.5$. (a, b): flow in the $z = 0$ plane. (c, d): flow in the $y = 0$ plane. $\bar{p} = (p - p_{ref})/\mu\omega$.

and 4d show that the pressure field in the system is qualitatively similar to that at $r/a = 1/15$. However, because of the stronger confinement by the horizontal wall, the pressure heterogeneity due to recirculation flow is enhanced and thus the pressure imbalance on the sphere's surface facing the vertical wall is enhanced (see Fig. 4b's inset). Meanwhile, the global flow around the sphere is weakened and thus the pressure imbalance on sphere's surface due to the interactions between the global flow and the center-fixed sphere is weakened. As a result, although this kind of pressure imbalance remains important on the sphere's surface facing away from the vertical wall, the region of surface where it dominates over the recirculation-induced pressure imbalance becomes smaller (see Fig. 4b's inset). As we shall see later, this change contributes to the reversal of hydrodynamic force on the sphere as r/a increases from 1/15 to 1/1.5.

Having studied the flow induced by a rotating sphere, we now evaluate the hydrodynamic force experienced by the sphere. Because the sphere rotates around the $z-$axis, the most significant hydrodynamic force acting on sphere is in the $x-$direction. Figure 5a shows the total hydrodynamic force F_x. We observe that, as r/a increases, F_x decreases and reverses sign at $r/a > 1/3$. In other words, as the confinement by the bottom wall increases, the actuation force decreases and ultimately reverses its direction.

To understand the origins of the observed evolution of F_x as a function of r/a, we first compute the components of F_x due to the pressure and viscous forces acting on the sphere's surface ($F_{x,p}$

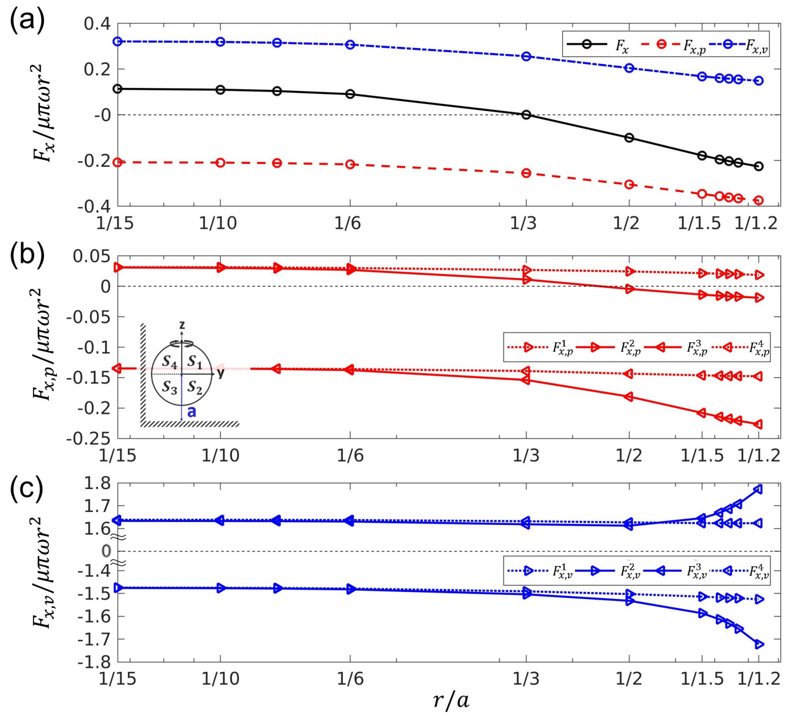

Figure 5: The hydrodynamic force acting on a rotating sphere positioned near walls of a channel with $W = 30r$. (a) The net force in the $x-$direction and its pressure and viscous components, (b-c) The $x-$direction pressure (b) and viscous (c) forces acting on surface S_1 to S_4 labeled in the inset of panel (b) (see Fig. 1a for a 3D view).

and $F_{x,v}$). As shown in Fig. 5a, at $r/a = 1/15$, when the sphere is essentially confined only by a semi-infinite vertical wall, $F_{x,p}$ is negative due to the large pressure difference across the sphere induced by the flow recirculation. As elucidated earlier,[46] the net viscous force on the sphere is in the positive $x-$direction and stronger than the pressure force. As r/a increases, both $F_{x,p}$ and $F_{x,v}$ decreases. Eventually, at large enough r/a (i.e., the sphere is positioned close to the bottom wall), pressure forces dominate the viscous forces, which differs qualitatively from the situation when the sphere is close to a semi-infinite vertical wall and leads to the reversal of F_x. To gain insight into the evolution of these pressure and viscous forces, we next decompose each force into that acting on the sphere's four surfaces labeled in Fig. 1b ($S_1, ..., S_4$). Hereafter, the pressure and viscous force on piece i of the sphere's surface are denoted as $F^i_{x,p}$ and $F^i_{x,v}$, respectively.

Figure 5b shows the variation of $F^{1\cdots4}_{x,p}$ as r/a increases (note that, throughout this work, r/b is fixed at $1/1.5$). While each force becomes more negative with increasing r/a, the decrease of $F^2_{x,p}$ and $F^3_{x,p}$ are far greater than that of $F^1_{x,p}$ and $F^4_{x,p}$. This is expected because the flow near surfaces facing toward the bottom wall (S_2 and S_3) is affected more significantly than that near surface facing away from the bottom wall (S_1 and S_4). The more negative $F^3_{x,p}$ at larger r/a is caused by the enhanced pressure buildup on the downstream of the sphere and the pressure depression on the upstream (cf. regions B and A in Fig. 4a and 4b), which is in turn caused by the increased confinement by the bottom wall as explained above. The decrease and eventual reversal of $F^2_{x,p}$ as r/a increases is expected. Specifically, as the confinement by the bottom wall increases, recirculation-induced pressure difference along the sphere in the streamwise direction (which produces a negative pressure force) is enhanced while global flow-induced pressure difference in the same direction (which produces a positive pressure force) is reduced as discussed above. To see this more clearly, we study the pressure field in the $z = -0.4r$ plane when $r/a = 1/15$ and $r/a = 1/1.5$. Figure 6 shows that, as r/a increases from 1/15 to 1/1.5, the pressure gradient along the surface facing toward the vertical wall increases, while that along the surface facing away from the vertical wall reverse direction, which is in line with the fact that $F^3_{x,p}$ becomes more negative while $F^2_{x,p}$ changes from positive to negative.

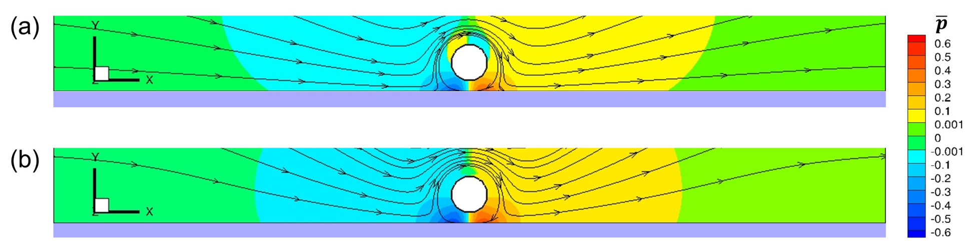

Figure 6: Pressure field and streamlines in the $z = -0.4r$ plane when $r/a = 1/15$ (a) and $r/a = 1/1.5$ (b).

Having analyzed the evolution of the pressure force $F_{x,p}$ acting on the sphere as r/a increases, we now analyze the evolution of the viscous force $F_{x,v}$. Figure 5c shows that, similar to the pressure forces, as r/a increases, only the viscous forces on the two surfaces facing the bottom wall (S_2 and S_3) change markedly. Because the sphere rotates in the clockwise direction, the viscous shear on S_2 and S_3 ($F^2_{x,v}$ and $F^3_{x,v}$) are in the negative and positive $x-$directions, respectively. As r/a increases, the strength of $F^2_{x,v}$ increases monotonically. This increase is caused by the enhanced velocity gradient $\nabla_r u_x$ (r denotes the sphere's radial direction) in region near surface S_2, which can be inferred from Fig. 3 as discussed earlier and is a result of the reduced distance between S_2 and the no-slip bottom wall. The enhanced $\nabla_r u_x$ can also be more clearly shown in Fig. 7, in which u_x along a ray OA passing through surface S_2 is shown at different r/a.

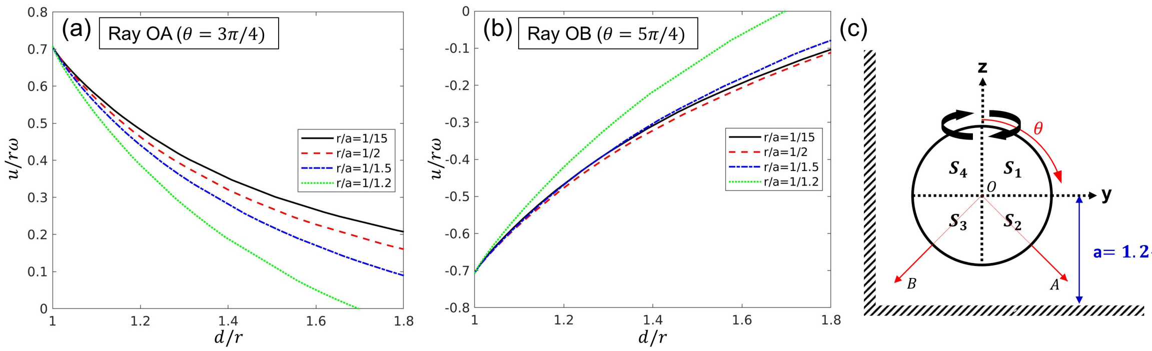

Figure 7: The variation of the $x-$component fluid velocity along rays OA and OB when the sphere is positioned at different height above the bottom wall. Both rays originate from the sphere's center and reside in the $x = 0$ plane. Rays OA (OB) passes through surface S_2 (S_3) and forms an angle of $3\pi/4$ ($5\pi/4$) with the positive $z-$axis.

The variation of $F^3_{x,v}$ with r/a however, is more complicated. As r/a increases from 1/15 to ∼1/2, $F^3_{x,v}$ decreases slightly; as r/a increases further, $F^3_{x,v}$ increases markedly. The initial, slight decrease of $F^3_{x,v}$ as the bottom wall moves toward to the sphere is mostly caused by the increase of the induced pressure gradient in the $x-$direction in the region between the sphere and the vertical wall. Specifically, although reducing the distance between the bottom wall and the sphere tends to increase $\nabla_r u_x$ near surface S_3 just like that near surface S_2, the increased pressure gradient tends to increase the fluid velocity in the region between surface S_3 and the vertical wall, thus reducing $\nabla_r u_x$ near surface S_3. The latter is supported by the velocity profile along ray OB passing through surface S_3 as shown in Fig. 7. As the bottom wall moves very close to the sphere (i.e., $r/a >\sim 1/2$), the enhancement of $\nabla_r u_x$ due to the proximity of the no-slip bottom wall to surface S_3 dominates the reduction of $\nabla_r u_x$ due to the enhanced pressure gradient, and $F^3_{x,v}$ increases markedly.

Overall, as r/a increases, the increase of the positive $F^3_{x,v}$ is weaker compared to the increase of the negative $F^2_{x,v}$, leading to a decrease of $F_{x,v}$. The weakening of the positive $F_{x,v}$ and strengthening of the negative $F_{x,p}$ with the increase of r/a eventually allows the pressure force to dominate the viscous force and makes the overall actuation force negative as shown in Fig. 5.

3.2 Sphere actuation in channels with symmetric top and bottom walls

We now fix the sphere at a distance $a = W/2$ from the bottom wall and vary W from $30r$ to $3r$ to study the effects of confinement by four walls on the actuation of the sphere (see Series 2 in Table 1 for details). In all studies, b is fixed at $1.5r$. The channel has a square cross-section, and the system geometry is symmetric in the $z-$direction. As in Section 3.1, we compute the flow in the system and measure the hydrodynamic force on the sphere in the $x-$direction.

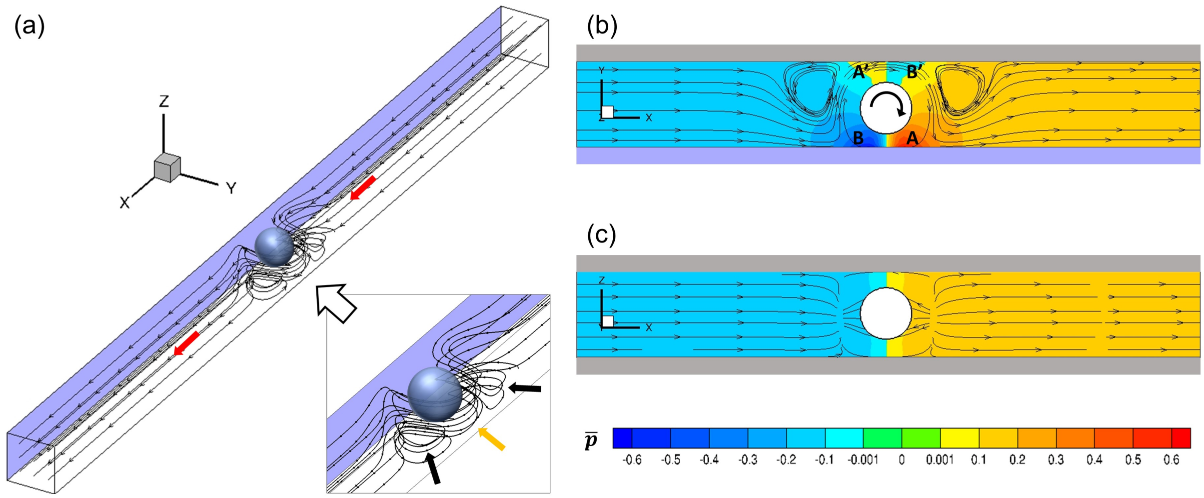

Figure 8: Flow in a channel-particle system with $a = W/2$, $b = 1.5r$, and $W = 3.5r$. (a) Sample streamlines. The sphere rotates around the $z-$axis in the clockwise direction. (b-c) Pressure field and streamlines in the $z = 0$ plane (b) and $y = 0$ plane (c) passing through the sphere's center (c). $\bar{p} = (p - p_{ref})/\mu\omega$.

We first study the flow field in a representative system where $a = W/2$ and $W = 3.5r$. Figure 8a shows the streamlines near the sphere. Similar to the situation shown in Fig. 3, a global flow in the $x-$direction is induced (marked by red arrows). However, because of the proximity of the two vertical walls, the fluids drawn from the sphere's one side are ejected onto the wall on the sphere's other side. The recirculation of fluids around the sphere's surface (marked by an orange arrow) induces two predominately horizontal recirculation bubbles near the vertical wall that is further away from the sphere (marked by two black arrows).

Figure 8b and 8c show the pressure field in the horizontal ($z = 0$) and vertical ($y = 0$) planes passing through the sphere's center. Because of the small W, both vertical walls affect the fluid flow. Such a flow rises the pressure in region A and lowers it in region B near the vertical wall that is closer to the sphere. At the same time, the flow rises the pressure in region A' and lowers it in region B' near the other vertical wall that is slightly further away from the sphere. Overall, the pressure imbalance between regions A and B is higher than that between regions A' and B'. Such kind of pressure imbalance occurs very close to the vertical walls – as shown in Fig. 8c, it is hardly noticeable in the $y = 0$ plane (i.e., $1.75r$ from the vertical walls). In addition to the above highly localized pressure heterogeneity, a pressure difference accompanying the global flow shown in Fig. 8 is developed along the channel: the pressure upstream of the sphere is lower and the pressure downstream of the sphere is higher. As discussed in Section 3.1, this pressure distribution creates a net force pushing the sphere in negative $x-$direction.

Figure 9a shows the variation of the hydrodynamic force acting on the sphere in the $x-$direction (F_x) as a function of r/W. As r/W increases, F_x decreases slightly, becomes negative at $r/W = 1/3.75$, then increases sharply and eventually reaches zero at $r/W = 1/3$. $F_x = 0$ at $r/W = 1/3$ is expected, because at this ratio, all four channel walls are distributed symmetrically with respect to the sphere. To understand the variation of F_x, we again decompose F_x into a pressure component $F_{x,p}$ and a viscous component $F_{x,v}$. Figure 9a shows that the variations of $F_{x,p}$ and $F_{x,v}$ with r/W are both similar to that of F_x, thus indicating that the changes of these forces contribute similarly to that of F_x. To understand these forces, we next decompose each pressure/viscous force into that acting on the sphere's four surfaces delineated in Fig. 1b and analyze these forces (note that, because the top and bottom walls are symmetric with respect to the sphere, the force acting on $S_1(S_3)$ is the same as that acting on $S_2(S_4)$). Figure 9b shows the variation of $F_{x,p}^{1\cdots4}$ as a function of r/W. As r/W increases from 1/30 to 1/10, $F_{x,p}^1$ to $F_{x,p}^4$ all decreases slightly; as r/W increases further, all four components decrease significantly; at $r/W >\sim 1/3.5$, all four components increase sharply as r/W increases.

The change of $F_{x,p}$ shown in Fig. 9a is a result of the modified pressure imbalance on the sphere's four surfaces as r/W increases. When r/W increases, the three non-shaded walls in Fig. 1a all move closer to the sphere. For $r/W <\sim 1/3.5$, such an enhanced confinement has a similar effect on $F_{x,p}^i (i = 1 \cdots 4)$ with the enhanced confinement of a sphere by the bottom wall (see Section 3.1 and Fig. 5b). Specifically, an increase of the confinement of the sphere by these walls enhances the recirculation-induced pressure imbalance near the sphere's surface facing the shaded vertical wall, which makes the negative $F_{x,p}^{3,4}$ more negative (see Fig. 9b), reduces $F_{x,p}^{1,2}$ and eventually makes it negative. Because the confinement by three walls is stronger than by one bottom wall of a channel corner, the variation of $F_{x,p}^i$ is stronger in the present case. For example, $F_{x,p}^2$ becomes negative at $r/a \sim 1/2.5$ in Fig. 5b while $F_{x,p}^2$ becomes negative at $r/W \sim 1/9$ (i.e., $r/a \sim 1/4.5$) in Fig. 9b. As r/W increases to $\sim 1/3.5$, the non-shaded vertical wall in Fig. 1a approaches the sphere to a distance comparable to that of the purple-shaded vertical wall. Therefore, the pressure imbalance across the space between by the sphere and the non-shaded vertical wall (cf. pressure

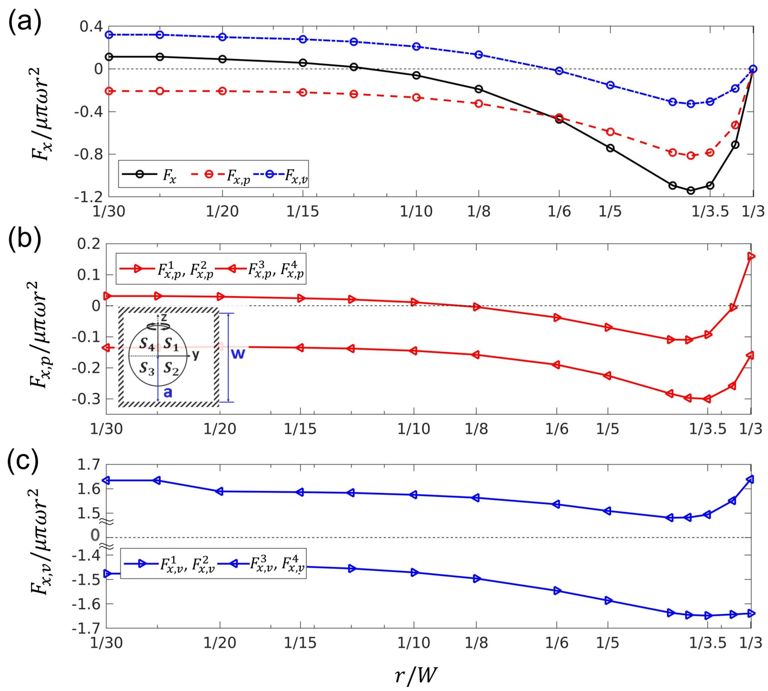

Figure 9: The hydrodynamic forces acting on a rotating sphere in square channels with different W ($a = W/2$ and $b = 1.5r$). (a) The net force in the $x-$direction and its pressure and viscous components, (b-c) The $x-$direction pressure (b) and viscous (c) forces acting on surface S_1 to S_4 labeled in the inset of panel (b) (see Fig. 1a for a 3D view).

imbalance between regions A' and B' in Fig. 8b) becomes more positive. Further increasing r/W enhances this pressure imbalance and eventually makes $F_{x,p}^{1,2}$ positive as shown in Fig. 9b.

Figure 9c shows the variation of $F_{x,v}^{1\cdots 4}$ as a function of r/W. As r/W increases from 1/30 to 1/3, $F_{x,v}^{3,4}$ decreases first and the increases sharply as r/W grows larger than 1/3.5. Meanwhile, $F_{x,v}^{1,2}$ generally becomes more negative as r/W increases but increases minutely at $r/W >\sim 1/3.5$. These trends are similar to those shown in Fig. 5c. As in Section 3.1, they can be attributed to the evolution of the velocity gradient near the sphere with the confinement by channel walls, which depends on the sphere's proximity to the no-slip walls and is also regulated by the pressure gradient along the gaps between the sphere and its adjacent walls. At $r/W = 1/3$, when the two vertical walls are distributed symmetrically with respect to the sphere, $F_{x,v}^{1,2}$ and $F_{x,v}^{3,4}$ become equal as expected.

3.3 Sphere actuation near walls of a narrow channel

In the previous section, we studied the actuation of a sphere in narrow channels by keeping the distance of the sphere to the top and bottom channel walls the same (i.e., $a = W/2$). Here, we relax this symmetric restriction by varying a and W independently (see Series 3 in Table 1). As before, b is fixed at $1.5r$ and the sphere rotates around the $x-$axis in the clockwise direction.

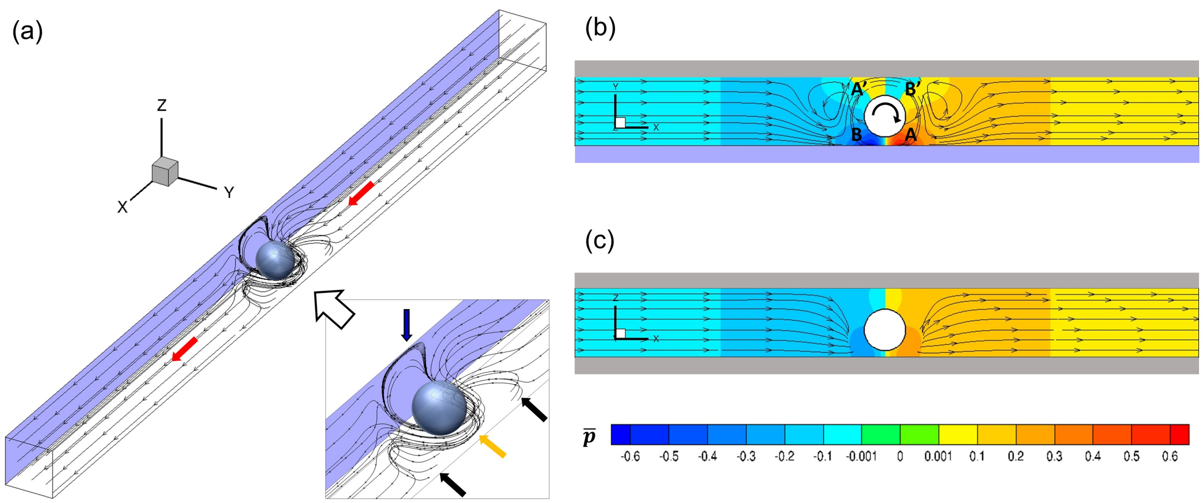

Figure 10: Flow in a channel-particle system with $a = 1.2r$, $b = 1.5r$, and $W = 3.5r$. (a) Sample 3D streamlines. The sphere rotates around the $z-$axis in the clockwise direction. (b-c) Pressure field and streamlines in the $z = 0$ plane (b) and $y = 0$ plane (c) passing through the sphere's center. $\bar{p} = (p - p_{ref})/\mu\omega$.

We first investigate the flow field in a representative case with $a = 1.2r$ and $W = 3.5r$. Figure 10a shows sample streamlines near the sphere. Like the flow field of Series 2 shown in Fig. 8, a global flow is induced in the $x-$direction (marked by red arrows), the fluids drawn from the sphere's one side are ejected onto the wall on the sphere's other side, and the recirculation of fluids around the sphere's surface (marked by an orange arrow) induces two horizontal recirculation bubbles (marked by two black arrows). However, unlike that shown in Fig. 8a, because the sphere is closer to the bottom wall than the top wall, a vertical recirculation (marked by a blue arrow) is created. Further, a recirculation around the sphere's surface (marked by an orange arrow) is formed near the bottom wall. Because of this recirculation, compared to those shown in 8c, the streamlines near the top wall are shifted toward the bottom wall as they approach the sphere (see Fig. 10c).

Figure 10b and 10c show the pressure field in the horizontal ($z = 0$) and vertical ($y = 0$)

planes passing through the sphere's center. The pressure field is similar to that in Series 2 with the same W (see Fig. 8b and c) in that two kinds of pressure heterogeneities exist. First, a pressure imbalance arises due to the interactions between the recirculating fluids around the sphere and the vertical walls. This pressure imbalance is localized near the vertical walls (e.g., in regions marked by A, B, A', and B' in Fig. 10b) and is hardly noticeable at a distance $\sim r$ away from the vertical walls. Second, as shown in Fig. 10c, a pressure difference caused by the global flow is created along the channel so that the pressure upstream of the sphere is lower while the opposite occurs in downstream. As mentioned earlier, this pressure distribution generates a net force pushing the sphere in the negative $x-$direction.

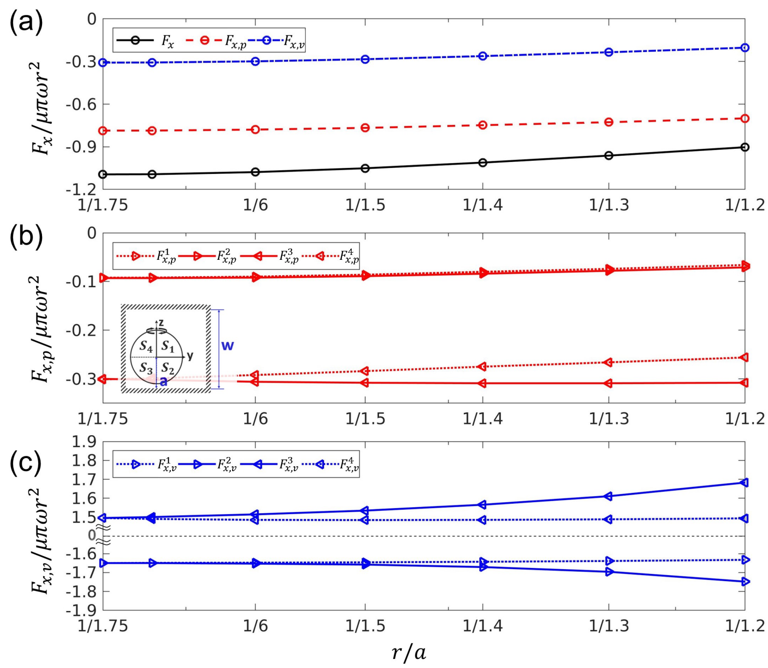

Figure 11: The hydrodynamic forces acting on a rotating sphere in square channels with different r/a ($W = 3.5r$ and $b = 1.5r$). (a) The net force in the $x-$direction and its pressure and viscous components, (b-c) The $x-$direction pressure (b) and viscous (c) forces acting on surface S_1 to S_4 labeled in the inset of panel (b) (see Fig. 1a for a 3D view).

Figure 11a shows the evolution of the hydrodynamic force and its components due to pressure and viscous forces as a function of r/a when W is fixed at $3.5r$. As r/a increases from 1/1.75 to 1/1.2, F_x, $F_{x,p}$, and $F_{x,v}$ all increase. The trend of these forces is opposite to that in the Series 1 study (where $W = 30r$) but is similar to that shown in the Series 2 study over the same range of

r/a (i.e., in the range of $1/3.5 < r/W < 1/2.4$ in Series 2 study). These differences highlight the importance of confinement by narrow channels on particle actuation. To understand the origins of the observed evolution of the hydrodynamic force as a function of r/a, we again decompose each force into that acting on the sphere's four surfaces labeled in Fig. 1b (S_1, ..., S_4).

Figure 11b shows that, as r/a increases, $F_{x,p}^{1,2,4}$ become less negative but $F_{x,p}^{3}$ changes little. These changes originate from the different responses of pressure in different regions near the sphere as it is shifted toward the bottom wall. As r/a increases, the sphere is confined more by the bottom channel wall while less confined by the top channel wall. The pressure field in the gap between the purple-shaded vertical wall and surface S_3 changes little, which is supported by the comparison of pressure fields in the $z = -0.6r$ plane for $r/a = 1/1.75$ and $1/1.2$ (see Fig. 12a and b). As such, $F_{x,p}^{3}$ changes little. On the other hand, as r/a increases, the local pressure imbalance between regions A' and B' becomes stronger (see Fig. 12a and b) and thus $F_{x,p}^{2}$ becomes less negative. A similar trend is found for the pressure imbalance along the gap between surface S_1 and its adjacent wall (see region A' and B' in Fig. 12c and d, where the pressure fields in the $z = 0.6r$ plane are compared). Thus $F_{x,p}^{1}$ also becomes less negative as r/a increases. A comparison of the pressure along the gap between surface S_4 and the purple-shaded wall shows that, as r/a increases, the pressure imbalance along the gap (e.g., between region A and B in Fig. 12c and d) decreases and hence $F_{x,p}^{4}$ becomes less negative.

Figure 11c shows the variation of $F_{x,v}^{1\cdots4}$ as r/a increases from $1/1.75$ to $1/1.2$. Similar to those shown in Section 3.1, as r/a increases, $F_{x,v}^{2}$ becomes more negative and $F_{x,v}^{3}$ becomes more positive. These behaviors and their origins are similar to those discussed in Section 3.1. Specifically, because the sphere is already very close to the no-slip bottom wall ($r/a > 1/2$), shifting the sphere closer to the no-slip bottom wall enhances the radial gradient of the $x-$velocity ($\nabla_r u_x$) and thus the magnitude of the viscous shear stress and $F_{x,v}^{2}$ and $F_{x,v}^{3}$. On the other hand, as r/a increases, $F_{x,v}^{1}$ and $F_{x,v}^{4}$ show little change. This is because, for the r/a considered here, $\nabla_r u_x$ near and on the sphere surface is affected primarily by the no-slip non-shaded vertical wall rather than by the top wall (note that the sphere rotates around the $z-$axis). Since the distance between the sphere and the vertical wall is fixed as r/a increases, $F_{x,v}^{1}$ and $F_{x,v}^{4}$ show little variation.

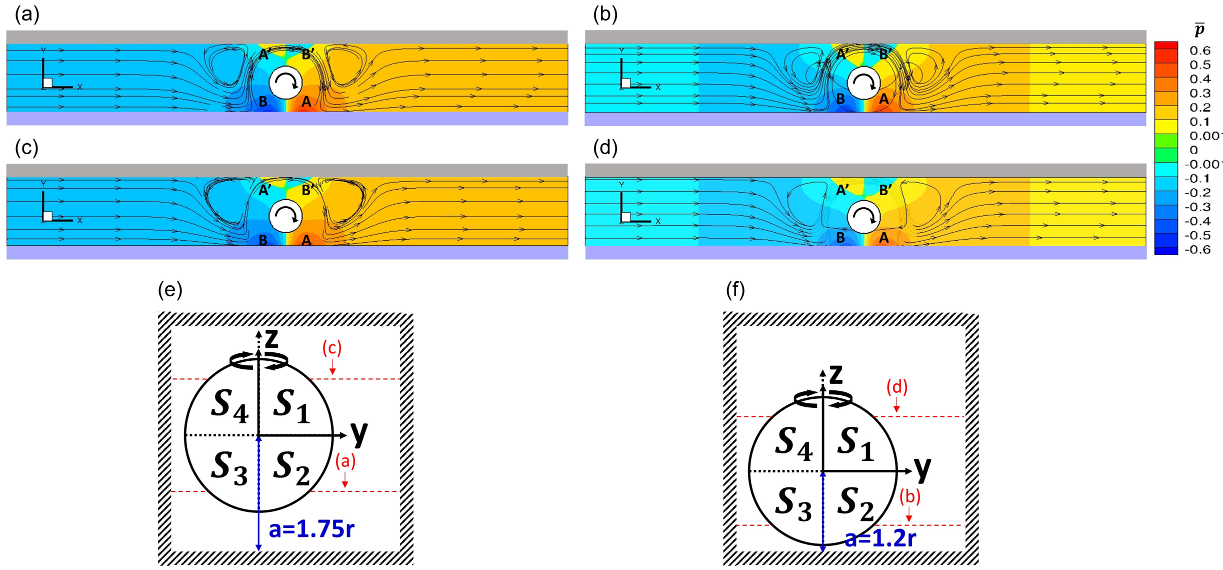

Figure 12: (a-b) Pressure field and streamlines in the $z = -0.6r$ plane when $r/a = 1/1.75$ (a) and $1/1.2$ (b). (c-d) Pressure field and streamlines in the $z = 0.6r$ plane when $r/a = 1/1.75$ (c) and $1/1.2$ (d). $W = 3.5r$ and $b = 1.5r$ in all cases. $\bar{p} = (p - p_{ref})/\mu\omega$.

4 CONCLUSIONS

In summary, the actuation of magnetic spheres confined inside square channels by a rotating magnetic field is studied using immersed-boundary lattice Boltzmann simulations. The sphere is positioned at a fixed distance from one of the vertical channel walls and rotates around the $z-$axis with a small rotational Reynolds number. The hydrodynamic actuation force acting on the sphere in the $x-$direction, F_x, is computed as a function of the channel width and the sphere's distance to the bottom channel wall.

Our simulations show that, in very wide channels, when a sphere is away from top and bottom walls, F_x is positive. F_x decreases and eventually reverses its direction as the sphere is shifted toward the channel corner. The opposite trend is discovered in channels that are sufficiently narrow. When the sphere is positioned midway between top and bottom walls, F_x decreases to become negative as the channel width decreases but then recovers to zero when all four channel walls are symmetric with respect to the sphere. These different trends are traced to the modulation of the flow in the channel, which features both recirculation near the sphere and a more global flow across the entire channel, by the confinement of channel walls. Such modulation is more complicated than that encountered when a rotating sphere is confined between two parallel walls.[46] In particular, the pressure heterogeneity near the sphere induced by fluid recirculation and global flow is modified greatly as the confinement by the four channel walls changes. The resulting pressure force can dominate the viscous force on the sphere and control the direction of F_x. The observed variations of F_x and their underlying mechanisms highlight the rich behavior of magnetic actuation inside microchannels and can be important for the application of magnetic actuation in microfluidic environment.

ACKNOWLEDGMENTS

The authors thank the ARC at Virginia Tech for generous allocation of computing time. R.Q. acknowledges support by the NSF under grant number 1808307.

References

(1) Purcell, E. M. Life at low Reynolds number. *American Journal of Physics* **1977**, *45*, 3–11.

(2) Yang, F.; Qian, S.; Zhao, Y.; Qiao, R. Self-diffusiophoresis of Janus catalytic micromotors in confined geometries. *Langmuir* **2016**, *32*, 5580–5592.

(3) Ma, F.; Yang, X.; Zhao, H.; Wu, N. Inducing propulsion of colloidal dimers by breaking the symmetry in electrohydrodynamic flow. *Physical review letters* **2015**, *115*, 208302.

(4) Qian, S.; Bau, H. H. Magneto-hydrodynamics based microfluidics. *Mechanics research communications* **2009**, *36*, 10–21.

(5) Driscoll, M.; Delmotte, B. Leveraging collective effects in externally driven colloidal suspensions: Experiments and simulations. *Current Opinion in Colloid & Interface Science* **2019**, *40*, 42–57.

(6) Yang, Z.; Zhang, L. Magnetic Actuation Systems for Miniature Robots: A Review. *Advanced Intelligent Systems* 2000082.

(7) Lim, B.; Vavassori, P.; Sooryakumar, R.; Kim, C. Nano/micro-scale magnetophoretic devices for biomedical applications. *Journal of Physics D: Applied Physics* **2016**, *50*, 033002.

(8) Barbillon, G.; Bosseboeuf, A.; Chun, K.; Ferrigno, R.; Français, O. *Engineering of Micro/Nano Biosystems*; Springer, 2020.

(9) Kirby, B. J. *Micro-and Nanoscale Fluid Mechanics: Transport in Microfluidic Devices*; Cambridge university press, 2010.

(10) Sing, C. E.; Schmid, L.; Schneider, M. F.; Franke, T.; Alexander-Katz, A. Controlled surface-induced flows from the motion of self-assembled colloidal walkers. *Proceedings of the National Academy of Sciences* **2010**, *107*, 535–540.

(11) Tottori, S.; Zhang, L.; Qiu, F.; Krawczyk, K. K.; Franco-Obregón, A.; Nelson, B. J. Magnetic helical micromachines: fabrication, controlled swimming, and cargo transport. *Advanced Materials* **2012**, *24*, 811–816.

(12) Khalil, I. S.; Tabak, A. F.; Hamed, Y.; Mitwally, M. E.; Tawakol, M.; Klingner, A.; Sitti, M. Swimming back and forth using planar flagellar propulsion at low Reynolds numbers. *Advanced Science* **2018**, *5*, 1700461.

(13) Yu, J.; Jin, D.; Chan, K.-F.; Wang, Q.; Yuan, K.; Zhang, L. Active generation and magnetic actuation of microrobotic swarms in bio-fluids. *Nature Communications* **2019**, *10*, 1–12.

(14) Rogowski, L. W.; Oxner, M.; Tang, J.; Kim, M. J. Heterogeneously flagellated microswimmer behavior in viscous fluids. *Biomicrofluidics* **2020**, *14*, 024112.

(15) Khalil, I. S.; Magdanz, V.; Simmchen, J.; Klingner, A.; Misra, S. Resemblance between motile and magnetically actuated sperm cells. *Applied Physics Letters* **2020**, *116*, 063702.

(16) El Alaoui-Faris, Y.; Pomet, J.-B.; Régnier, S.; Giraldi, L. Optimal actuation of flagellar magnetic microswimmers. *Physical Review E* **2020**, *101*, 042604.

(17) Zhu, L.; Huang, W.; Yang, F.; Yin, L.; Liang, S.; Zhao, W.; Mao, L.; Yu, X.; Qiao, R.; Zhao, Y. Manipulation of Single Cells Using a Ferromagnetic Nanorod Cluster Actuated by Weak AC Magnetic Fields. *Advanced Biosystems* **2019**, *3*, 1800246.

(18) Tierno, P.; Golestanian, R.; Pagonabarraga, I.; Sagués, F. Controlled swimming in confined fluids of magnetically actuated colloidal rotors. *Physical Review Letters* **2008**, *101*, 218304.

(19) Martinez-Pedrero, F.; Ortiz-Ambriz, A.; Pagonabarraga, I.; Tierno, P. Colloidal microworms propelling via a cooperative hydrodynamic conveyor belt. *Physical Review Letters* **2015**, *115*, 138301.

(20) Wang, Q.; Yu, J.; Yuan, K.; Yang, L.; Jin, D.; Zhang, L. Disassembly and spreading of magnetic nanoparticle clusters on uneven surfaces. *Applied Materials Today* **2020**, *18*, 100489.

(21) Sprinkle, B.; van der Wee, E. B.; Luo, Y.; Driscoll, M. M.; Donev, A. Driven dynamics in dense suspensions of microrollers. *Soft Matter* **2020**,

(22) Helgesen, G. Magnetic propulsion of microspheres at liquid-glass interfaces. *Journal of Applied Physics* **2018**, *123*, 064902.

(23) Zhang, S.; Wang, Y.; Onck, P.; den Toonder, J. A concise review of microfluidic particle manipulation methods. *Microfluidics and Nanofluidics* **2020**, *24*, 1–20.

(24) Martínez-Pedrero, F.; Tierno, P. Advances in colloidal manipulation and transport via hydrodynamic interactions. *Journal of Colloid and Interface Science* **2018**, *519*, 296–311.

(25) Erb, R. M.; Martin, J. J.; Soheilian, R.; Pan, C.; Barber, J. R. Actuating soft matter with magnetic torque. *Advanced Functional Materials* **2016**, *26*, 3859–3880.

(26) Elgeti, J.; Winkler, R. G.; Gompper, G. Physics of microswimmers—single particle motion and collective behavior: a review. *Reports on Progress in Physics* **2015**, *78*, 056601.

(27) Van Reenen, A.; de Jong, A. M.; den Toonder, J. M.; Prins, M. W. Integrated lab-on-chip biosensing systems based on magnetic particle actuation–a comprehensive review. *Lab on a Chip* **2014**, *14*, 1966–1986.

(28) Tierno, P. Recent advances in anisotropic magnetic colloids: realization, assembly and applications. *Physical Chemistry Chemical Physics* **2014**, *16*, 23515–23528.

(29) Rikken, R. S.; Nolte, R. J.; Maan, J. C.; van Hest, J. C.; Wilson, D. A.; Christianen, P. C. Manipulation of micro-and nanostructure motion with magnetic fields. *Soft Matter* **2014**, *10*, 1295–1308.

(30) Martinez-Pedrero, F.; Navarro-Argemí, E.; Ortiz-Ambriz, A.; Pagonabarraga, I.; Tierno, P. Emergent hydrodynamic bound states between magnetically powered micropropellers. *Science advances* **2018**, *4*, eaap9379.

(31) Driscoll, M.; Delmotte, B.; Youssef, M.; Sacanna, S.; Donev, A.; Chaikin, P. Unstable fronts and motile structures formed by microrollers. *Nature Physics* **2017**, *13*, 375–379.

(32) Delmotte, B.; Driscoll, M.; Chaikin, P.; Donev, A. Hydrodynamic shocks in microroller suspensions. *Physical Review Fluids* **2017**, *2*, 092301.

(33) Kaiser, A.; Snezhko, A.; Aranson, I. S. Flocking ferromagnetic colloids. *Science Advances* **2017**, *3*, e1601469.

(34) Xiao, Z.; Wei, M.; Wang, W. A review of micromotors in confinements: Pores, channels, grooves, steps, interfaces, chains, and swimming in the bulk. *ACS applied materials & interfaces* **2018**, *11*, 6667–6684.

(35) Singh, A.; Li, J.; Jiang, X.; Hernández-Ortiz, J. P.; Jaeger, H. M.; de Pablo, J. J. Shape induced segregation and anomalous particle transport under spherical confinement. *Physics of Fluids* **2020**, *32*, 053307.

(36) Liu, P.; De Folter, J. W.; Petukhov, A. V.; Philipse, A. P. Reconfigurable assembly of superparamagnetic colloids confined in thermo-reversible microtubes. *Soft Matter* **2015**, *11*, 6201–6211.

(37) Alonso-Matilla, R.; Saintillan, D. Microfluidic flow actuation using magnetoactive suspensions. *EPL (Europhysics Letters)* **2018**, *121*, 24002.

(38) Sherman, Z. M.; Pallone, J. L.; Erb, R. M.; Swan, J. W. Enhanced diffusion and magnetophoresis of paramagnetic colloidal particles in rotating magnetic fields. *Soft matter* **2019**, *15*, 6677–6689.

(39) Satoh, A.; Chantrell, R. W. Application of the dissipative particle dynamics method to magnetic colloidal dispersions. *Molecular Physics* **2006**, *104*, 3287–3302.

(40) Kang, T. G.; Hulsen, M. A.; Anderson, P. D.; den Toonder, J. M.; Meijer, H. E. Chaotic mixing induced by a magnetic chain in a rotating magnetic field. *Physical Review E* **2007**, *76*, 066303.

(41) Kang, T. G.; Hulsen, M. A.; den Toonder, J. M.; Anderson, P. D.; Meijer, H. E. A direct simulation method for flows with suspended paramagnetic particles. *Journal of Computational Physics* **2008**, *227*, 4441–4458.

(42) Lagger, H. G.; Breinlinger, T.; Korvink, J. G.; Moseler, M.; Di Renzo, A.; Di Maio, F.;

Bierwisch, C. Influence of hydrodynamic drag model on shear stress in the simulation of magnetorheological fluids. *Journal of Non-Newtonian Fluid Mechanics* **2015**, *218*, 16–26.

(43) Rossi, E.; Ruiz-Lopez, J. A.; Vazquez-Quesada, A.; Ellero, M. Dynamics and rheology of a super-paramagnetic chain suspension under the combined effect of a shear flow and a rotating magnetic field. *Soft Matter* **2021**,

(44) Krishnamurthy, S.; Yadav, A.; Phelan, P.; Calhoun, R.; Vuppu, A.; Garcia, A.; Hayes, M. Dynamics of rotating paramagnetic particle chains simulated by particle dynamics, Stokesian dynamics and lattice Boltzmann methods. *Microfluidics and Nanofluidics* **2008**, *5*, 33–41.

(45) Han, K.; Feng, Y.; Owen, D. Modelling of magnetorheological fluids with combined lattice Boltzmann and discrete element approach. *Communications in Computational Physics* **2010**, *7*, 1095.

(46) Fang, W.-Z.; Ham, S.; Qiao, R.; Tao, W.-Q. Magnetic Actuation of Surface Walkers: The Effects of Confinement and Inertia. *Langmuir* **2020**,

(47) Cheng, R.; Huang, W.; Huang, L.; Yang, B.; Mao, L.; Jin, K.; ZhuGe, Q.; Zhao, Y. Acceleration of tissue plasminogen activator-mediated thrombolysis by magnetically powered nanomotors. *ACS Nano* **2014**, *8*, 7746–7754.

(48) Goldman, A. J.; Cox, R. G.; Brenner, H. Slow viscous motion of a sphere parallel to a plane wall—I Motion through a quiescent fluid. *Chemical Engineering Science* **1967**, *22*, 637–651.

(49) Zeng, L.; Balachandar, S.; Fischer, P. *Wall-induced forces on a rigid sphere at finite Reynolds number*; 2004.

(50) Liu, Q.; Prosperetti, A. Wall effects on a rotating sphere. *Journal of Fluid Mechanics* **2010**, *657*, 1.

(51) Fang, C.; Sun, S.; Qiao, R. Structure, thermodynamics, and dynamics of thin brine films in oil–brine–rock systems. *Langmuir* **2019**, *35*, 10341–10353.

(52) Feng, Z.-G.; Michaelides, E. E. Robust treatment of no-slip boundary condition and velocity updating for the lattice-Boltzmann simulation of particulate flows. *Computers & Fluids* **2009**, *38*, 370–381.

(53) Kang, S. K.; Hassan, Y. A. A comparative study of direct-forcing immersed boundary-lattice Boltzmann methods for stationary complex boundaries. *International Journal for Numerical Methods in Fluids* **2011**, *66*, 1132–1158.

(54) Zhang, D.; Papadikis, K.; Gu, S. Three-dimensional multi-relaxation time lattice-Boltzmann model for the drop impact on a dry surface at large density ratio. *International Journal of Multiphase Flow* **2014**, *64*, 11–18.

(55) d'Humieres, D. Multiple–relaxation–time lattice Boltzmann models in three dimensions. *Philosophical Transactions of the Royal Society of London. Series A: Mathematical, Physical and Engineering Sciences* **2002**, *360*, 437–451.

(56) Krüger, T.; Kusumaatmaja, H.; Kuzmin, A.; Shardt, O.; Silva, G.; Viggen, E. M. The lattice Boltzmann method. *Springer International Publishing* **2017**, *10*, 4–15.

(57) Guo, Z.; Zheng, C.; Shi, B. Discrete lattice effects on the forcing term in the lattice Boltzmann method. *Physical Review E* **2002**, *65*, 046308.